A&A 592, A24 (2016)
DOI: 10.1051/0004-6361/201527690

Astronomy & Astrophysics

Surface-effect corrections for the solar model

Z. Magic[1,2] and A. Weiss[3]

[1] Niels Bohr Institute, University of Copenhagen, Juliane Maries Vej 30, 2100 Copenhagen, Denmark
e-mail: magic@nbi.dk
[2] Centre for Star and Planet Formation, Natural History Museum of Denmark, Øster Voldgade 5−7, 1350 Copenhagen, Denmark
[3] Max-Planck-Institut für Astrophysik, Karl-Schwarzschild-Str. 1, 85741 Garching, Germany

Received 3 November 2015 / Accepted 24 May 2016

ABSTRACT

Context. Solar p-mode oscillations exhibit a systematic offset towards higher frequencies due to shortcomings in the 1D stellar structure models, in particular, the lack of turbulent pressure in the superadiabatic layers just below the optical surface, arising from the convective velocity field.
Aims. We study the influence of the turbulent expansion, chemical composition, and magnetic fields on the stratification in the upper layers of the solar models in comparison with solar observations. Furthermore, we test alternative ⟨3D⟩ averages for improved results on the oscillation frequencies.
Methods. We appended temporally and spatially averaged ⟨3D⟩ stratifications to 1D models to compute adiabatic oscillation frequencies that we then tested against solar observations. We also developed depth-dependent corrections for the solar 1D model, for which we expanded the geometrical depth to match the pressure stratification of the solar ⟨3D⟩ model, and we reduced the density that is caused by the turbulent pressure.
Results. We obtain the same results with our ⟨3D⟩ models as have been reported previously. Our depth-dependent corrected 1D models match the observations to almost a similar extent as the ⟨3D⟩ model. We find that correcting for the expansion of the geometrical depth and the reducing of the density are both equally necessary. Interestingly, the influence of the adiabatic exponent Γ_1 is less pronounced than anticipated. The turbulent elevation directly from the ⟨3D⟩ model does not match the observations properly. Considering different reference depth scales for the ⟨3D⟩ averaging leads to very similar frequencies. Solar models with high metal abundances in their initial chemical composition match the low-frequency part much better. We find a linear relation between the p-mode frequency shift and the vertical magnetic field strength with $\delta\nu_{nl} = 26.21 B_z$ [μHz/kG], which is able to render the solar activity cycles correctly.

Key words. convection – hydrodynamics – Sun: helioseismology – Sun: activity – Sun: magnetic fields – Sun: oscillations

1. Introduction

The Sun shows p-mode oscillations that are due to the stochastic excitation by turbulent convection. Certain frequencies are damped and others are amplified, which leads to a characteristic set of frequencies observed on the Sun. In helioseismology, observed oscillation frequencies are compared with theoretical model predictions to probe the solar structure below the optical surface (Christensen-Dalsgaard 2002). In 1D stellar structure calculations, convection is modelled with the mixing length theory (Böhm-Vitense 1958), hence the mismatch in the superadiabatic region (SAR) just below the optical surface leads to systematic residuals for the high-frequency modes. These are termed surface effects. To account correctly for convection, and in particular, for the turbulent pressure, we need to employ 3D hydrodynamic models, where convection emerges from first principles (Stein & Nordlund 1998). Rosenthal et al. (1999) found that appending a mean stratification from a 3D model (Stein & Nordlund 1998) to a 1D solar model (Christensen-Dalsgaard et al. 1996) can indeed reduce the surface effects by providing additional support through turbulent pressure and a concomitant expansion of the acoustic cavity at the surface by 150 km, which in turn reduces the oscillation frequencies. Sonoi et al. (2015) calibrated surface-effect corrections for other stars than the Sun from 3D models. In the present work, we repeat the efforts of Rosenthal et al. (1999) with the solar model from the STAGGER GRID (Magic et al. 2013a) and study the solar surface effects in detail.

2. Methods

2.1. Theoretical models

We considered the solar mean ⟨3D⟩ model taken from the STAGGER GRID (see Magic et al. 2013b, for more details), which was computed with the STAGGER code. In the 3D models, the equation-of-state (EOS) from Mihalas et al. (1988) is used, and the opacities are taken from the MARCS package (Gustafsson et al. 2008). The numerical resolution is 240^3 and twelve opacity bins were considered for the radiative transfer.

For the 1D model we took a standard solar calibrated model (including atomic diffusion) computed with the GARSTEC stellar evolution code (see Weiss & Schlattl 2008; Magic et al. 2010, for more details). In the 1D model, we used the EOS by OPAL 2005 (Rogers et al. 1996) for higher temperatures, while for the lower temperatures we extended the EOS by those from Mihalas et al. (1988), for consistency between the 3D and 1D models. The opacity in the GARSTEC model is a combination of results from OPAL (Iglesias & Rogers 1996) and Ferguson et al. (2005) for higher and lower temperatures, respectively. In all models, we assumed the solar chemical composition by Asplund et al. (2009), except for the oscillation frequencies in Sect. 3.3.

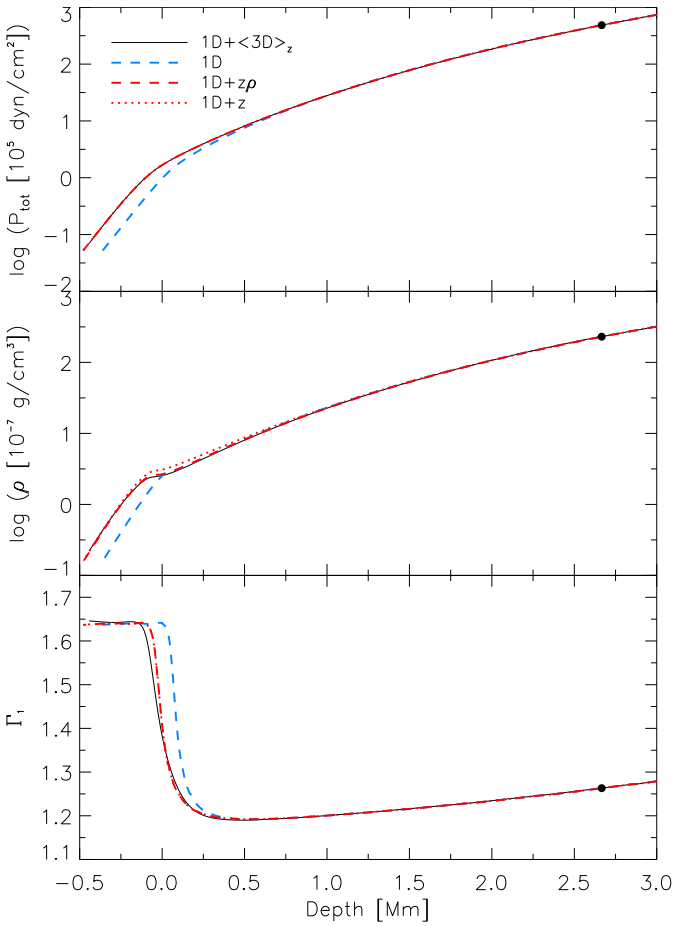

Fig. 1. Total pressure, density, and adiabatic exponent for the 1D model combined with the $\langle 3D \rangle_z$ model. We marked the location of the transition between $\langle 3D \rangle_z$ and 1D (black dot). In addition to the original 1D model (blue dashed line), we also show the values of the 1D model corrected for both the geometrical depth and density (red dashed line) and corrected for the depth alone (red dotted line).

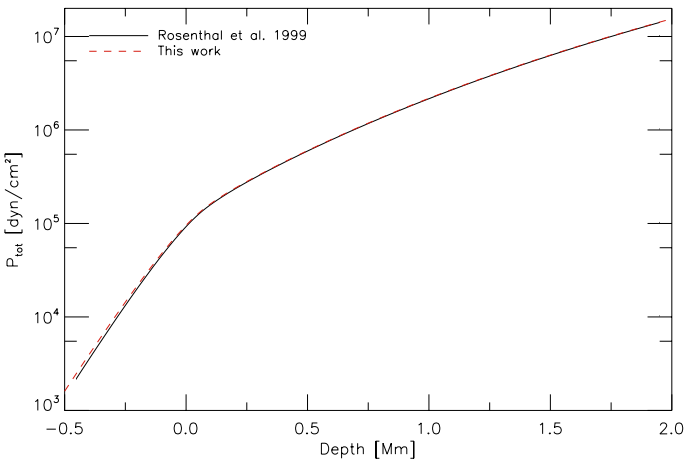

Fig. 2. Total pressure vs. depth averaged from the 3D models of this work and compared with Rosenthal et al. (1999).

Table 1. Overview of the different mean $\langle 3D \rangle$ models and their reference depth scale for the horizontal or spatial averaging.

Symbol	Spatial averages over layers of constant
$\langle 3D \rangle_z$	geometrical depth
$\langle 3D \rangle_{\rm up}$	geometrical depth for the upflows
$\langle 3D \rangle_{\rm dn}$	geometrical depth for the downflows
$\langle 3D \rangle_L$	(pseudo-Lagrangian) geometrical depth
$\langle 3D \rangle_m$	column mass density
$\langle 3D \rangle_{p_{\rm tot}}$	total pressure
$\langle 3D \rangle_\tau$	acoustic depth

The pressure stratification of our $\langle 3D \rangle$ model shown in Fig. 1 is very similar to the gas gamma model by Rosenthal et al. (1999). Our 3D model exhibits a slightly higher pressure stratification only above the optical surface (see Fig. 2). This is probably owed to the differences in the input physics, the treatment of the radiative transfer, and numerical resolution (theirs is lower with $100^2 \times 82$). When we compared our solar model with models with higher numerical resolution (480^3 and $960^2 \times 480$), we found the differences in the stratifications of the models to be minute. Comparisons with other numerical codes (CO5BOLD and MURAM) also result in very similar temperature and pressure stratifications (see Figs. 4 and 5 in Beeck et al. 2012). These comparisons mean that our temperature and pressure stratifications are reliable.

To compute the theoretical eigenmode frequencies, we employed the adiabatic oscillation code ADIPLS (Christensen-Dalsgaard 2008). Here, the independent variables are the total pressure, $p_{\rm tot}$, the density, ρ, and the adiabatic exponent, Γ_1 (see Fig. 1). Rosenthal et al. (1999) computed oscillation frequencies with the spatially and temporally averaged adiabatic exponent, to which they referred as the gas gamma model. They also worked with a reduced gamma model. Based on the differences between the gas gamma and the reduced gamma model, they found a difference of $\sim 10\,\mu$Hz at higher frequencies. However, their reduced gamma model disagreed with observations because the adiabatic exponent was too low. Therefore, we used the spatial and temporal averages of Γ_1 in the present study (gas gamma model). We also computed the reduced gamma, $\Gamma_1^{\rm red} = \left\langle p_{\rm gas}\Gamma_1 \right\rangle / \left\langle p_{\rm gas} \right\rangle$, but we found only very little difference to the plain values of Γ_1. Since the surface effects are less dependent on the angular degree, we considered the lowest mode ($l = 0$) in comparison with the observational data provided by GOLF measurements (Lazrek et al. 1997).

2.2. Temporal and spatial averaging

To compute the spatially and temporally averaged mean $\langle 3D \rangle$ is nontrivial, as we showed in Magic et al. (2013a) for spectroscopy. For the application in helio- and asteroseismology, we similarly needed to test and find a reference depth-scale to average independent variables in the most suitable way. Therefore, we considered seven different averages (see Table 1) that we explain in the following. The geometrical average (denoted with z) is used by default, since it fulfils the hydrostatic equilibrium. We computed geometrical averages separated into up- and downflows (denoted with up and dn), based on the sign of the vertical velocity component. Furthermore, we also used pseudo-Lagrangian averages (denoted with L) that were spatially averaged over geometrical depth and temporally averaged by mapping to a fixed column mass scale to remove the contribution of the p-mode oscillations from the spatial averages (see Trampedach et al. 2014). Optical depth can be ruled out as a reference depth scale, because the averages are then correlated to the temperature (see Magic et al. 2013b, for more details).

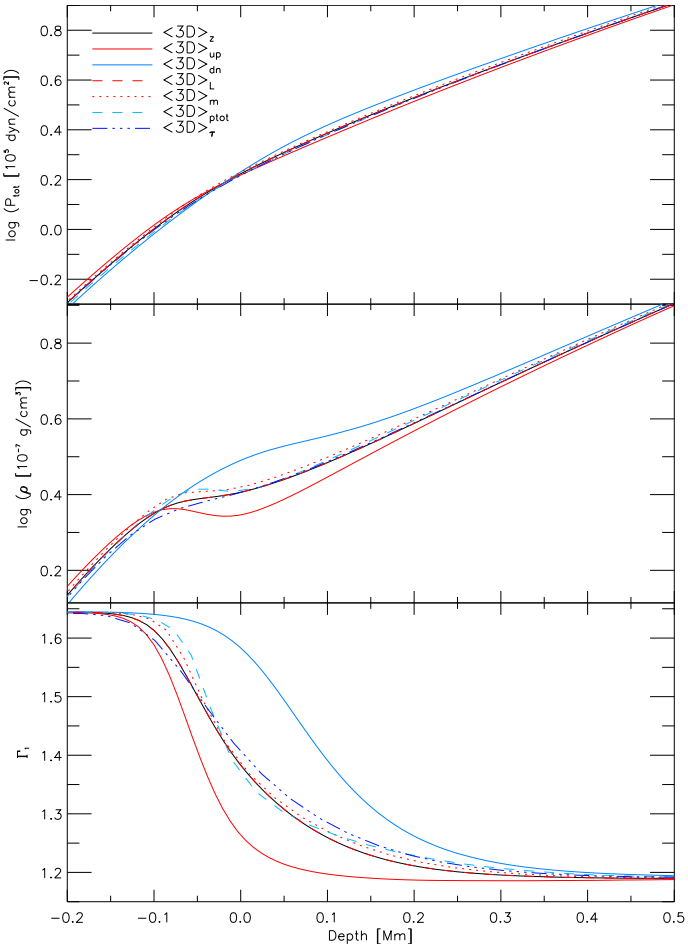

Fig. 3. Similar to Fig. 1, but showing models with different ⟨3D⟩ averages. The geometrically averaged model, z (solid black line), is identical to the model shown in Fig. 1 (black solid line). Inward of a depth of roughly −0.1 Mm, the averages of the upflows, $\langle 3D\rangle_{up}$, are the lowest curves, while the downflows, $\langle 3D\rangle_{dn}$, are the uppermost curves in all three panels.

We considered averages over layers of constant column mass density

$$m = \int \rho \mathrm{d}z, \tag{1}$$

acoustic depth

$$\tau = \int \frac{1}{c_s} \mathrm{d}z, \tag{2}$$

and total pressure $p_{\rm tot}$. In the photosphere, where the fluctuations are strongest, we can expect differences between the different averages that might alter the oscillation frequencies. In Fig. 3 we show the total pressure, density, and adiabatic exponent for the different ⟨3D⟩ averages. The different averages exhibit small differences for the independent variables, except for the averages for the up- and downflows, which show larger differences than the other averages. In particular, this is the case for the density and adiabatic exponent, while the total pressure shows only smaller differences. The averages of the upflows depict the hot, ascending granules, while the downflows depict the cold, descending intergranular lane at the optical surface. The pseudo-Lagrangian averages (red dashed lines) are indistinguishable from the geometrical averages (solid black lines). As mentioned above the pseudo-Lagrangian averages are spatially averaged over geometrical depth and differ only in the temporal averaging, which seems to have very little effect on the stratification. Furthermore, we note that the averages over the column mass density are clearly distinct from the former because they employ the column mass density as the reference depth scale.

2.3. Including the effects of the turbulent expansion

The 3D models are very shallow, therefore we need to append the ⟨3D⟩ models to a 1D model to study the effect on the p-mode oscillations. To do this, we employed two methods (Sects. 2.3.1 and 2.3.2) to include the effects of the turbulent expansion on the 1D model. The first method is similar to the one by Rosenthal et al. (1999), and we appended a ⟨3D⟩ model to a 1D model. In the second method, we expanded the geometrical depth in the top layers of the 1D model to achieve the same total pressure stratification as for the ⟨3D⟩ model.

2.3.1. Appending the ⟨3D⟩ on the 1D model

We appended the $\langle 3D\rangle_z$ model averaged over layers of constant geometrical depth, where the zero-point was set to coincide with the optical surface, that is, $\langle \tau_{\rm Ross}\rangle = 0$, to the 1D model at the bottom of the $\langle 3D\rangle_z$ model. To do this, we considered the total pressure in the deepest layers of the $\langle 3D\rangle_z$ model, $p_{\rm tot}^{\rm bot}$, and matched the difference in geometrical depth

$$\Delta z^{\rm bot} = z^{\rm 3D}\left(p_{\rm tot}^{\rm bot}\right) - z^{\rm 1D}\left(p_{\rm tot}^{\rm bot}\right), \tag{3}$$

which is a single depth-independent correction value. We obtained for $\Delta z^{\rm bot}$ a shift of 81.6 km. Next, we shifted the geometrical depth of the $\langle 3D\rangle_z$ models for the difference, that is, $z^{\rm 3D,shifted} = z^{\rm 3D} + \Delta z^{\rm bot}$. Finally, we interpolated the independent variables $p_{\rm tot}$, ρ, Γ_1 from the $\langle 3D\rangle_z$ to the geometrical depth of the 1D model ($z^{\rm 1D}$) and merged both models into a single model. The appended model is expanded relative to the 1D model and the stratifications of $p_{\rm tot}$, ρ and Γ_1 are visibly modified at the top (see Fig. 1). The global radius is increased by the total elevation at the surface with $\Delta z(0) = 105$ km, as determined in Sect. 2.3.2. This value can be compared to the findings by Rosenthal et al. (1999) of 150 km. The correction of the depth at the bottom of the ⟨3D⟩ model, $\Delta z^{\rm bot} = 81.6$ km, is necessary, since the 1D model compensates the missing turbulent pressure and the higher temperatures at the surface of the 3D model with a higher pressure scale height below the optical surface. The different temperature stratification in the 3D model is a result of the temperature sensitivity of the opacity and inhomogeneities of the granulation (see Sect. 5.2 in Rosenthal et al. 1999). On the other hand, without the depth correction, the 3D and 1D model would exhibit a discontinuous transition at the connection point. Both of the latter are important to improve the oscillation frequency, as we show below. We refer to the $\langle 3D\rangle_z$ model appended to 1D model as the 3D model.

2.3.2. Depth-dependent structure corrections

Instead of appending a ⟨3D⟩ structure to the 1D model, we employed depth and density corrections directly on the 1D stellar structure as well. The idea behind this is very simple: we wish to find a depth correction that expands the geometrical depth, so that the same pressure-depth relation of the 3D model is realised for the 1D model. To do this, we determined the difference in geometrical depth, which is necessary to yield the same

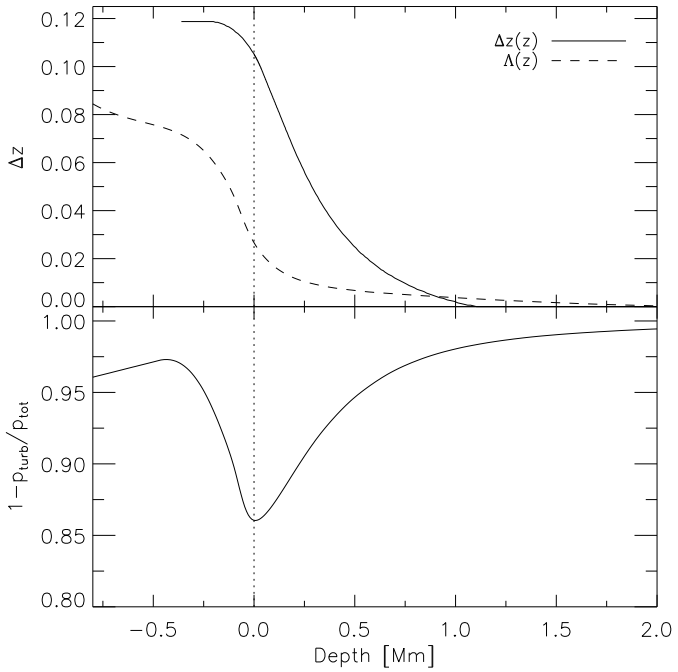

Fig. 4. Depth-dependent corrections for the geometrical depth, Δz, and corrections of the density, $1 - p_{\rm turb}/p_{\rm tot}$, in the 1D solar model (*top and bottom panel*, respectively). Furthermore, we show the turbulent elevation from Eq. (7) (dashed line in *the top panel*). The location of the optical surface is indicated (vertical dotted line).

pressure stratification. The depth-dependent correction factor is determined by

$$\Delta z\,(z) \quad = \quad z^{\rm 3D}\left(p_{\rm tot}^{\rm 3D}\right) - z^{\rm 1D}\left(p_{\rm tot}^{\rm 1D}\right), \tag{4}$$

which can expand the geometrical depth of the 1D model to the match the total pressure stratification of the ⟨3D⟩ model. We note that the geometrical depth of the 3D model, $z^{\rm 3D}$, in Eq. (4) is corrected for the depth shift at the bottom with Eq. (3), that is, $z^{\rm 3D,shifted} = z^{\rm 3D} + \Delta z^{\rm bot}$. Furthermore, we note that in contrast to Eq. (3), here $\Delta z\,(z)$ is depth dependent. We neglected negative depth corrections below the optical surface for consistency. Then, the resulting correction was applied to the geometrical depth, that is, $z^* = z + \Delta z\,(z)$, which leads to an expansion of the entire stellar structure at the top alone. This results in an extension of the solar radius at the optical surface, meaning that from Eq. (4) we obtain $\Delta z\,(0) = 105$ km (see Fig. 4).

The corrected geometrical depth deviates from the hydrostatic equilibrium in the SAR, therefore, we corrected the density stratification by reducing it by the ratio of the turbulent pressure and the total pressure:

$$\rho^* \quad = \quad \rho\,(1 - p_{\rm turb}/p_{\rm tot})\,, \tag{5}$$

since the missing hydrostatic support from the $p_{\rm turb}$ is balanced by higher densities in the 1D model. On the other hand, we can also determine the density stratification, which fulfils the hydrostatic equilibrium. Then, this correction leads to the identical density stratification as given by the ⟨3D⟩ model, since the corrected geometrical depth results in an identical pressure stratification with depth by construction, and the equation of hydrostatic equilibrium (Eq. (6)) is only fulfilled by a unique density stratification.

In Fig. 4 we show both the depth and density correction. The corrected 1D model including z^* and ρ^* is also shown in Fig. 1 (red dashed lines), which is very close to the ⟨3D⟩ stratification. The density stratification without the correction (Eq. (5)) is only slightly higher, and only minor differences are visible for Γ_1. As we show in Sect. 3.1, both have effects of very different magnitudes on the oscillation frequencies.

The hydrostatic equilibrium can be retrieved by averaging the momentum equation, which results in

$$\frac{{\rm d}(\bar{p}_{\rm th} + \bar{\rho}\bar{u}_z^2)}{{\rm d}z} \quad = \quad \bar{\rho} g_z, \tag{6}$$

with $\bar{u}_z$ being the density-weighted average of the vertical velocity component (often referred to as turbulent velocity) and $p_{\rm turb} = \rho u_z^2$ the turbulent pressure, which is an additional pressure support against gravity. The density correction stems mostly from the vertical component of the velocity field. By separating the support from $p_{\rm turb}$ and integrating for the depth, we obtain the turbulent elevation

$$\Lambda\,(z) \quad = \quad -\int_{-\infty}^{z} \frac{{\rm d}p_{\rm turb}}{\rho g}, \tag{7}$$

which depicts the expansion caused by the turbulent velocity field that is due to convection in SAR (Trampedach 1997). In Fig. 4 we also show the turbulent elevation (dashed line). This has a shape similar to $\Delta z\,(z)$, but the amplitude of the total elevation at the surface is mismatched with $\Lambda\,(0) = 26$ km, in contrast to $\Delta z\,(0) = 105$ km. This difference propagates into a larger difference in oscillation frequencies, rendering the use $\Lambda\,(z)$ directly as futile, meaning that the resulting frequencies are unable to match the observations (see Fig. 5a).

To append ⟨3D⟩ models to 1D structures is straightforward in the case of solar parameters; for other stars, such as red giants or turn-off stars, however, this becomes more difficult, because the gradients of 3D and 1D models often do not match. A possible solution of this dilemma is to include the missing turbulent pressure in the 1D model. To do this, we can use the ratio between the turbulent and total pressure, which quickly drops close to zero below the SAR. We corrected for the density first with Eq. (5) and for the ratio in pressures from the ⟨3D⟩ model. Then, we integrated for the geometrical depth under hydrostatic equilibrium with Eq. (6), which expanded the geometrical depth. To obtain good results, we needed to apply a constant factor of 3/2 to the ratio of pressures in Eq. (5). We emphasize that the advantage of this approach is that the ⟨3D⟩ model does not need to be matched at the bottom, which results in a more continuous structure; but this is a subject of a forthcoming work.

3. Oscillation frequencies

In Fig. 5a we show the computed oscillation frequencies in comparison with the observations. The ⟨3D⟩ model (black solid line) clearly exhibits smaller residuals than the 1D solar model, thereby verifying that it renders the SAR more accurately than the 1D model. We also show a 1D model, in which we expanded the geometrical depth with the turbulent elevation (dashed line in Fig. 4) and corrected the density for hydrostatic equilibrium. The expansion improves the 1D model, but it is not enough. A comparison of our ⟨3D⟩ model results with Rosenthal et al. (1999) leads to the same residuals in the oscillation frequencies (see Fig. 5b) because the pressure stratifications are almost the same, as we mentioned above in Sect. 2.1.

3.1. Corrected structures

To determine the actual influences of the corrections in depth, density and adiabatic exponent, we corrected them individually.

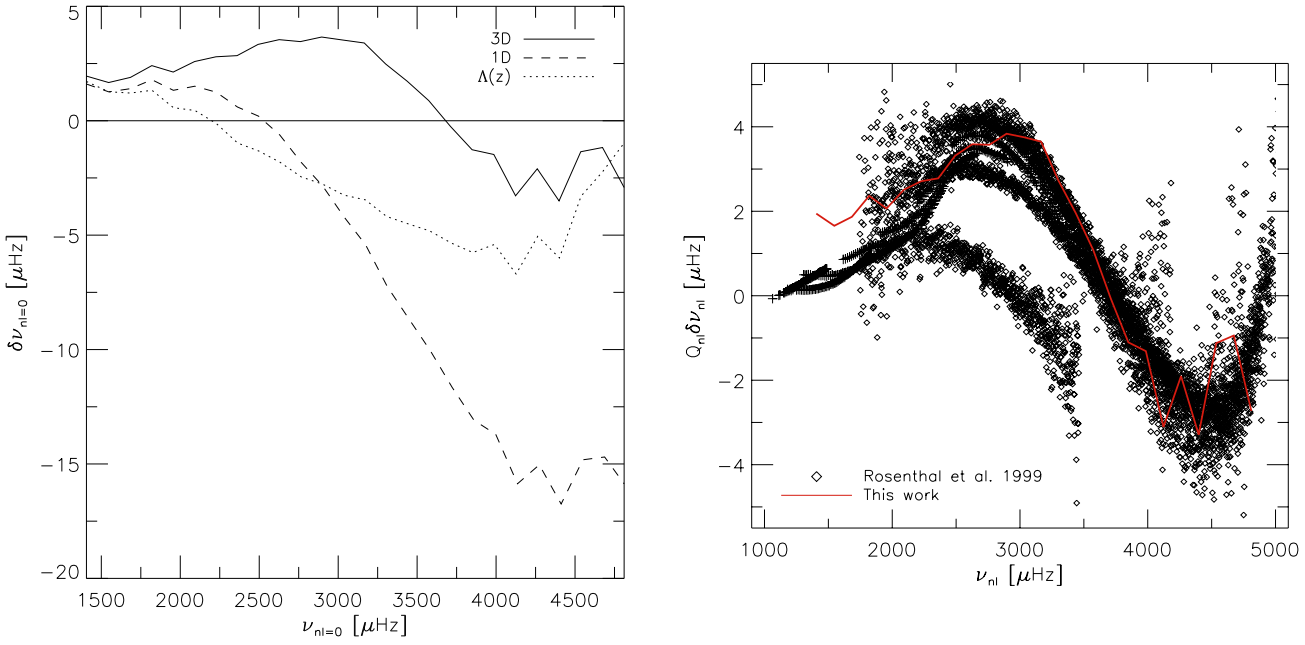

Fig. 5. a) Frequency residuals vs. frequency for two solar models in comparison with solar observations for a low-degree mode with $l = 0$. The differences are retrieved by $\delta\nu_{nl} = \nu_{nl}^{\rm obs} - \nu_{nl}^{\rm mod}$. Shown are the 3D corrected model (black solid line), the standard 1D solar model (dashed lines) and a 1D model expanded with the turbulent elevation (dotted lines; see Eq. (7)). The height of zero differences is indicated (horizontal solid line). **b)** We also show the residuals for different modes scaled with Q_{nl} resulting from a solar model corrected with 3D model (GGM: gas gamma model) published by (Rosenthal et al. 1999; black symbols) in comparison with our result for $l = 0$ (red solid line).

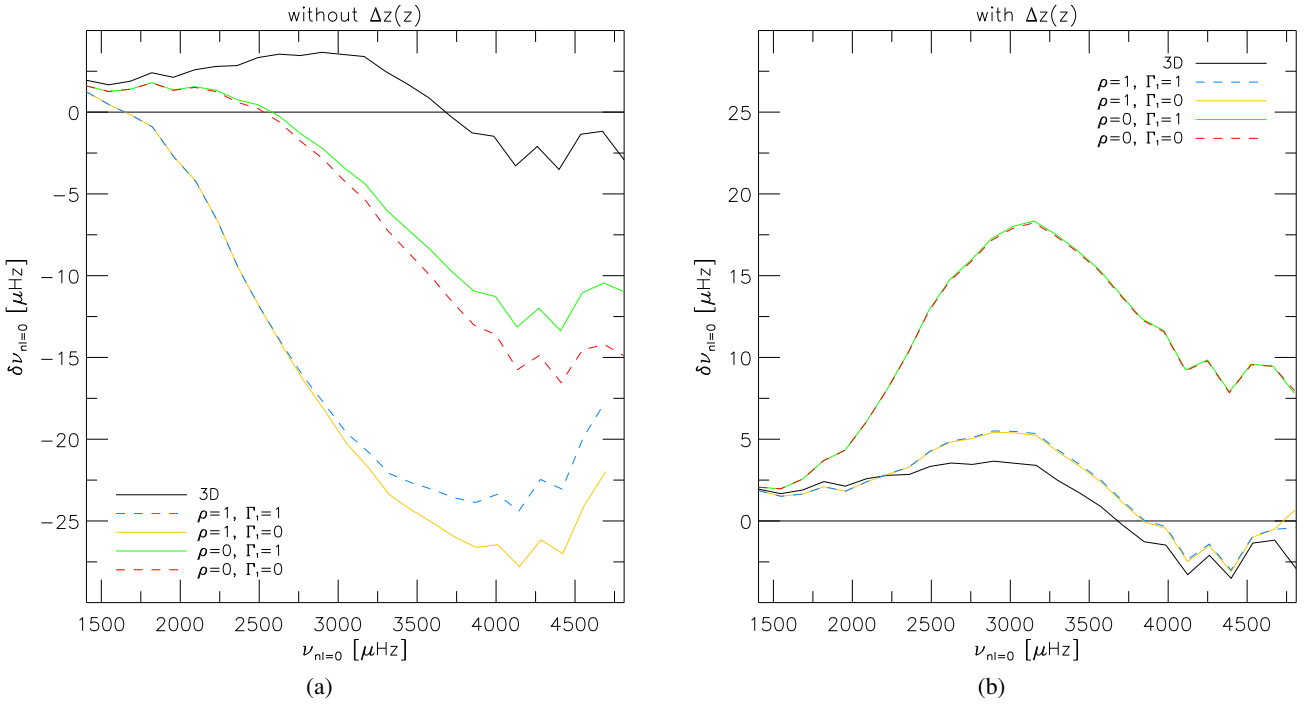

Fig. 6. a) Similar to Fig. 5a, but showing 1D models without any geometrical depth corrections $\Delta z\,(z)$, but with corrections in density and adiabatic exponent. **b)** Similar to Fig. 6a, but here the 1D models include the geometrical depth corrections $\Delta z\,(z)$. Note the differences in the ordinates. For comparison we also show the 3D model (black solid line) in both panels. See text for more details.

First we consider the models without any depth correction $\Delta z\,(z)$ given by Eq. (4) (see Fig. 6a). In this panel, all four of the 1D models show large, negative systematic offsets that reach values of between 12 to 28 μHz at the high-frequency end. When we employed only the density correction to the 1D model (orange solid line), we found that the mismatch was substantially worsened to ~28 μHz. In addition, adopting the adiabatic exponent alone from the ⟨3D⟩ model in the 1D model gives the best

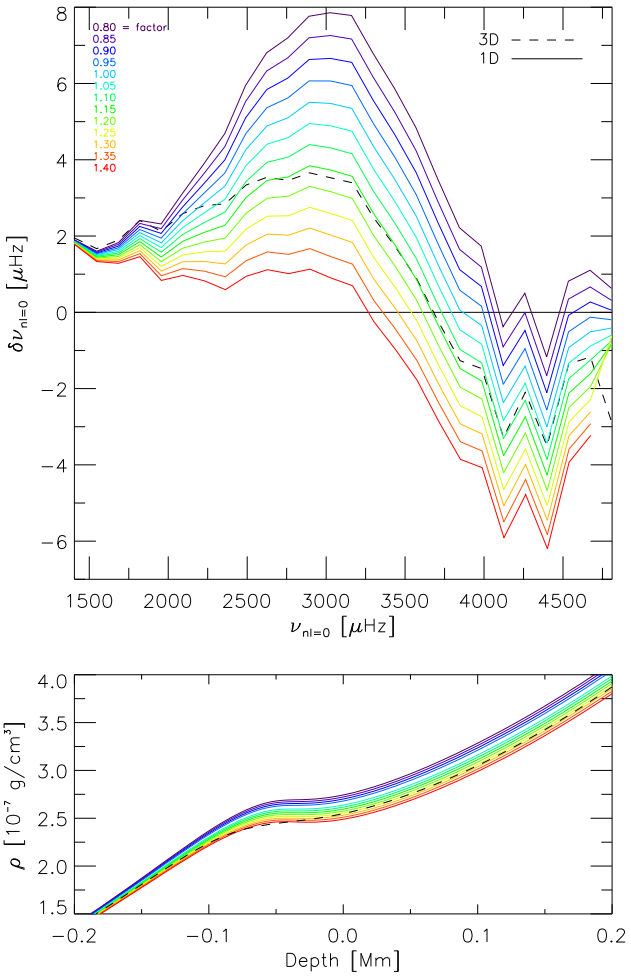

Fig. 7. *Top panel*: similar to Fig. 5a, but showing models with different density corrections. The line with the density correction of 1.0 is the same as shown in Fig. 6b (blue dashed line). *Bottom panel*: density profiles. In both panels, the 3D-corrected model is also shown for comparison (black dashed line).

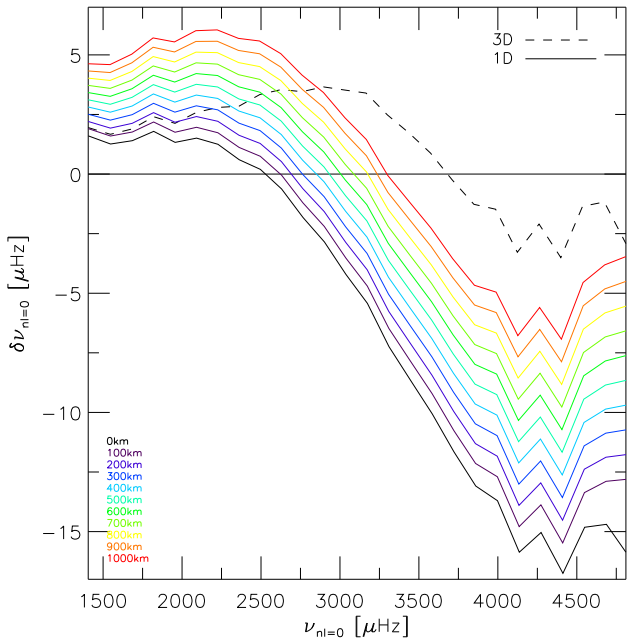

Fig. 8. Similar to Fig. 5a, but showing 1D models without any corrections. Instead, only the radii are expanded. The 3D-corrected model is also shown for comparison (black dashed line).

match (green solid line), but it does not improve the mismatch significantly. The change in the adiabatic exponent affects the oscillation frequencies only slightly with a difference of ∼5 μHz at higher frequencies that increases above ∼3000 μHz (between $\Gamma_1 = 1$ and $\Gamma_1 = 0$) compared to the density correction (between $\rho = 1$ and $\rho = 0$). This yields a difference of ∼10 μHz (see Fig. 6a). The adiabatic exponent for the ⟨3D⟩ and 1D models is shown in Fig. 1 (see blue dashed line in the bottom panel).

Only by adopting the depth correction $\Delta z\,(z)$ given in Eq. (4) and the density correction (Eq. (5)), can we achieve a significant improvement in the oscillation frequencies in comparison with observations (see Fig. 6b). The differences in the frequencies between the 1D model and the observations are reduced by expanding the structure. It is obvious, however, that the density correction is crucial for a closer match (blue dashed and orange solid lines; we note that these two lines overlap in Fig. 6b). The correction of Γ_1 alone hardly changes anything (blue dashed and green solid line), which is consistent with the very small differences in the Γ_1 stratification between the ⟨3D⟩ and 1D model (red lines in bottom panel of Fig. 1).

The density corrections seem small (see red dotted line in Fig. 1), but their effect on the frequencies is very strong. This illustrates that the frequencies are very sensitive to the density stratification in the SAR immediately below the optical surface. The density needs to be reduced because the missing turbulent pressure is compensated for by higher densities. We varied the density correction (Eq. (5)) with a constant scaling factor between 0.8 and 1.4, to show the effect on the p-mode frequency, which is shown in Fig. 7. Again, the changes in the frequencies are very strong, indicating the importance of the density stratification on the oscillations. A smaller density correction increases the residuals between observations and theoretical model, in particular around ∼3000 μHz, while a larger density correction decreases the residuals, but at higher frequencies the mismatch is more pronounced. The net effect of these changes in the residuals is to shift the frequency range over which the residuals are small from high frequencies for the largest density corrections to lower frequencies for the smallest density corrections.

An expansion of the global radius of the model alone will extend the acoustic cavity and it will also result in increases in the modelled frequencies. However, such an isolated change to the model will not resolve the mismatch, since the structures of the surface layers are unchanged (see Fig. 8). The relative differences between model and observations are shifted to higher values, but the overall shape is preserved. Therefore, none of the models with expanded radius can provide a good match to the observations. This illustrates that the depth-dependent corrections from the ⟨3D⟩ model in the SAR of the solar structure are as important as the expansion of the radius alone. The expansion of the radius has to be included, but by itself it is not sufficient to correct for the surface effects.

Instead of correcting the frequencies for the surface-effects, we can also directly correct the surface layers of a 1D model. As shown in Fig. 6b, a depth-dependent expansion of the geometrical depth and a correction of the density are necessary steps. Furthermore, from asteroseismic observations, we can infer the correct structure of stellar structure model-independently models by finding the right corrections around the critical surface layers.

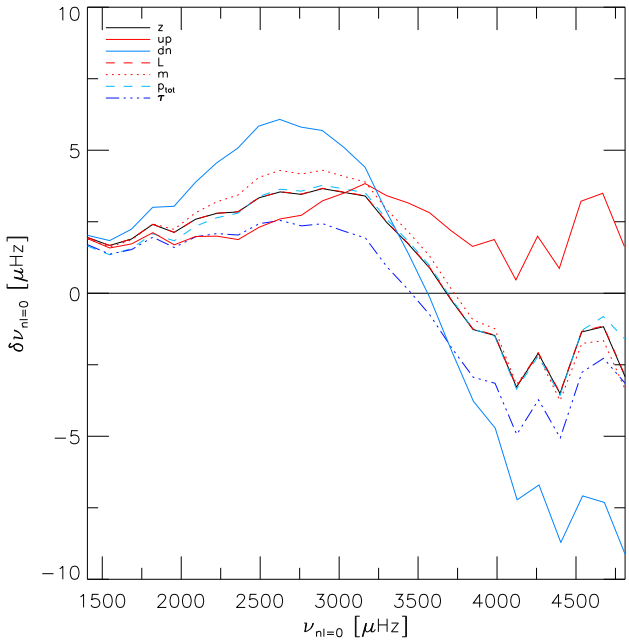

Fig. 9. Similar to Fig. 5a, but showing models with different ⟨3D⟩ averages.

3.2. Different averages

The question arises about the effect of different averaging methods of the 3D model structure on the *p*-mode frequencies. In Fig. 3 we compared the radial profiles of pressure, density, and adiabatic exponent that we obtained using seven different averaging methods of the 3D model structure. We found above in Sect. 2.2 that most of the different averages depict only small changes, which also results in only small changes of the oscillation frequencies as shown in Fig. 9. The geometrical averages for the up- and downflows exhibit the largest difference in the density and adiabatic exponent immediately below the optical surface. The upflows depict lower densities, because the hotter granules are lighter than the turbulent downdrafts in the intergranular lane. The ⟨3D⟩ model for the downflows leads to the highest mismatches with observations compared to the other ⟨3D⟩ model. On the other hand, the ⟨3D⟩ model of the upflows leads to the best agreement with observations, since the residuals are almost a straight line. In particular, the agreement at higher frequencies is much better, which is mainly due to the adiabatic exponent. One reason for this result might be the adiabatic nature of the frequency calculations, since the averages over the upflows are closer to the adiabatic stratification. The pseudo-Lagrangian averages are indistinguishable from the plain geometrical averages. The averages on the acoustic depth are slightly closer to observations below ∼3000 μHz, but in higher frequencies the mismatch is larger. The averages on constant layers of column mass density and total pressure are about the same as on geometrical depth.

3.3. Chemical composition

Next we consider the influence of the chemical composition on the oscillations frequency. In Fig. 10 we show frequencies computed with solar 1D models assuming solar chemical compositions different from our standard composition (Asplund et al. 2009, AGS09), while the abundances in the ⟨3D⟩ model were fixed (the difference would be only minor). We considered the

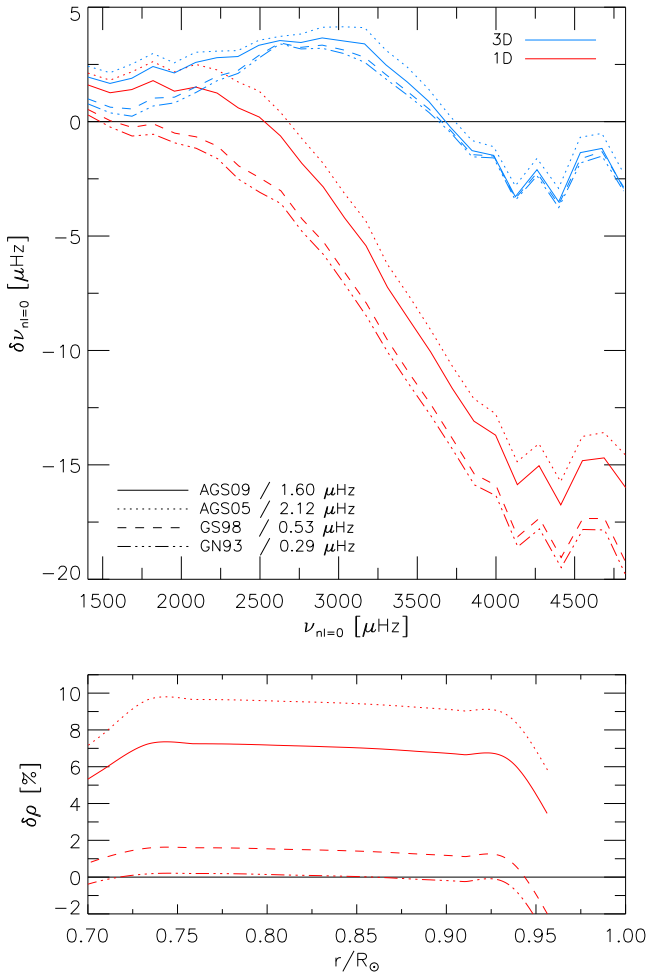

Fig. 10. *Top panel*: similar to Fig. 5a, but showing models with different abundances. Shown are uncorrected 1D models (red lines) and 3D-corrected models (blue lines). The latter are the different 1D models, but appended with the same 3D model, which is why they converge towards higher frequencies and differ towards lower frequencies. We also note the low-frequency mismatch for the individual abundances. *Bottom panel*: differences in density compared to inferred ρ from observations (Basu et al. 2009).

solar chemical compositions by Asplund et al. (2005, AGS05), Grevesse & Sauval (1998, GS98), and Grevesse & Noels (1993, GN93). The modes at low frequency are affected by a change in chemical composition. For chemical compositions assuming higher metallicity, the low frequencies match the solar observations better. With the most metal-poor composition AGS05 we find a mismatch of 2.12 μHz at the low-frequency end (1500 μHz), while for most of the metal-rich composition GN93 we find the best match with much lower residuals with 0.3 μHz. The different chemical compositions change the structure in the solar models. The models with higher metallicity match the interior better, which is also known for the inferred sound speed and density in the convection zone (see Fig. 10).

3.4. Magnetic field

We also computed solar 3D MHD models with vertical magnetic field strengths of up to 1500 kG. We included monolithic vertical fields in initially hydrodynamic models and appointed the same vertical magnetic field to the gas entering the numerical

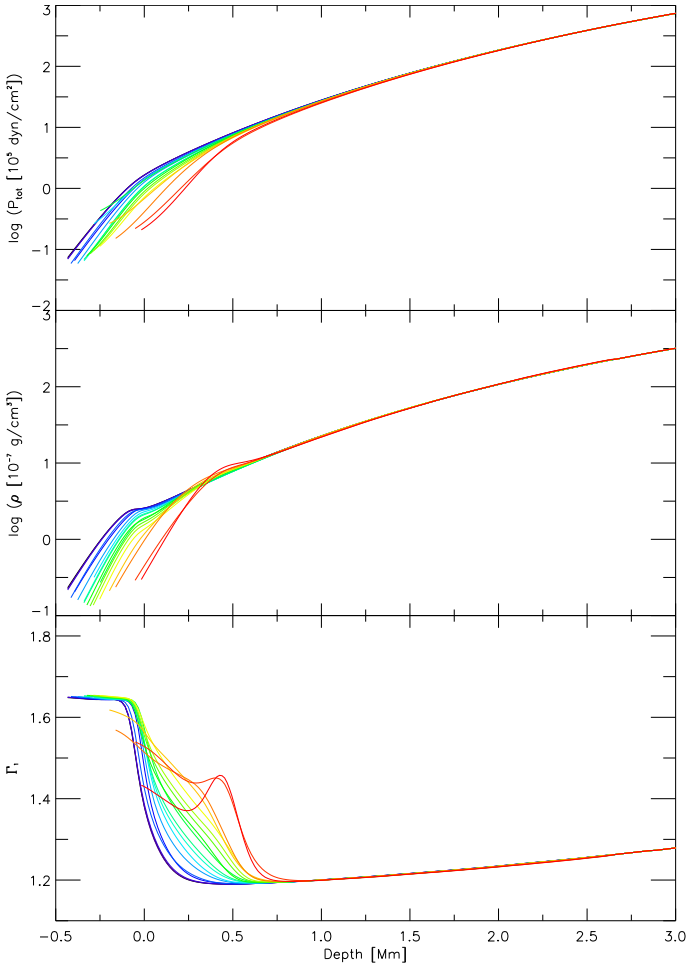

Fig. 11. Comparison of total pressure, density and adiabatic exponent for ⟨3D⟩ models with different magnetic field strengths.

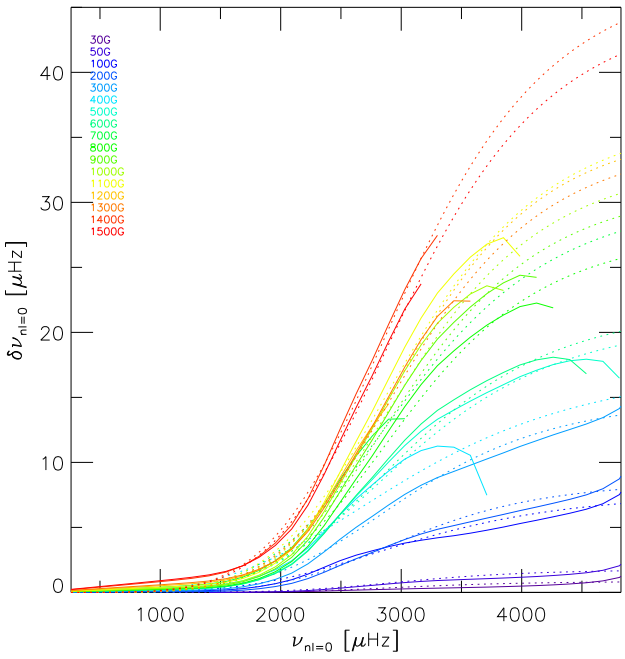

Fig. 12. Frequency differences between ⟨3D⟩ models with different magnetic field strengths compared to non-magnetic case, i.e. $\delta\nu = \nu_{XG} - \nu_{0G}$. We also performed a modified Lorentzian fit (dotted lines).

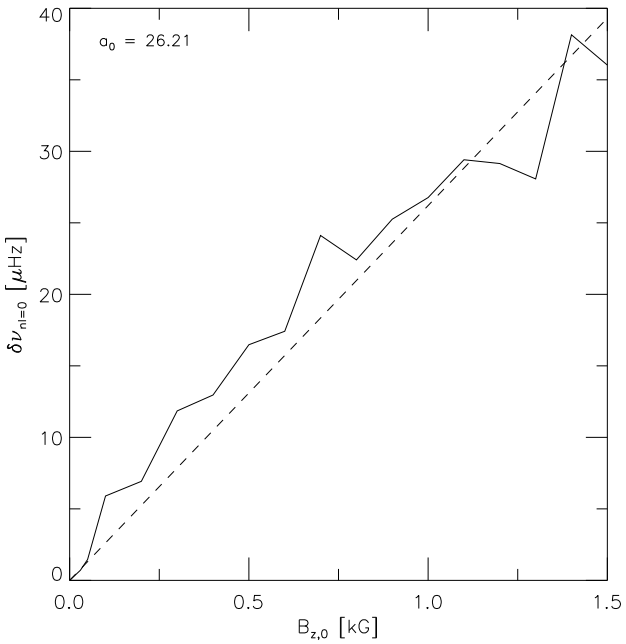

Fig. 13. Frequency shifts determined at $\nu_{nl} = 4000\,\mu$Hz from the modified Lorentzian fits (Fig. 12), shown against the magnetic field strength (black solid line). We also show the linear fit (dashed line).

box at the bottom. Then, we evolved the simulations until the MHD models reached the quasi-stationary state. From the subsequent models we determined spatial and temporal averages. We truncated the initial hydrodynamic solar model slightly at the top and we reduced the numerical resolution to 120^3 to keep computational costs low. The magnetic inhibition of the flow increases with the magnetic field strength through the coupling of the velocity field with the magnetic field through the Lorentz force in the SAR. This leads to significant changes in the stratification of the solar model. Owing to the magnetic inhibition of convection, the mean temperature, density, and pressure are reduced significantly in the surface layers (see Fig. 11). Furthermore, the turbulent pressure is reduced, and the magnetic pressure increasingly evacuates the plasma. In this way the optical surface is depressed by 400 km in the model with 1.5 kG, which affects the frequencies by shortening the acoustic cavity, which in turn increases the oscillation frequencies. We appended the magnetic ⟨3D⟩ models to the 1D solar model to test the influence of the magnetic field on the oscillation frequencies. We show in Fig. 12 the corresponding comparisons with the non-magnetic model. As a consequence of the depression of the optical surface, the frequencies are enhanced with increasing field strength. At high field strength with 1.5 kG, the p-mode frequencies are increased by almost ~45 μHz at the high-frequency end. We also determined the relation between magnetic field strength and the frequency shift, $\delta\nu_{nl} \propto B_z$ (see Figs. 12 and 13). We fitted the relative differences with the modified Lorentzian function

$$\delta\nu/\nu_{\max} = \alpha\left(1 - 1/\left[1 + (\nu/\nu_{\max})^{\beta}\right]\right) \quad (8)$$

with $\nu_{\max} = 3090\,\mu$Hz (see Sonoi et al. 2015) and determined the shift at $\nu_{nl} = 4000\,\mu$Hz. We found the following response relation for the magnetic field

$$\delta\nu_{nl} = 26.21 B_z, \quad (9)$$

where the vertical magnetic field strength is given in units of kG (see Fig. 13). We note that the frequency shift considered at

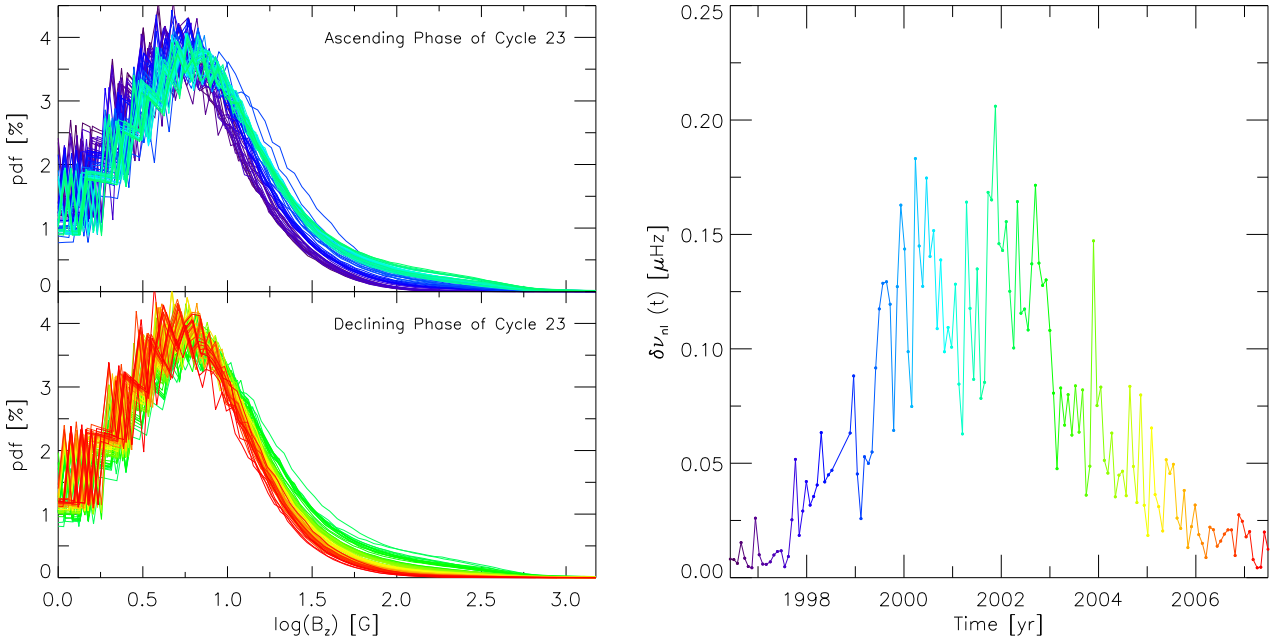

(a) (b)

Fig. 14. a) Histogram of magnetic field strength determined from synoptic SOHO/MID maps for the ascending and declining phases (*top* and *bottom panel*, respectively). **b)** The integrated frequency shift, $\delta\nu_{nl}\,(t)$ (Eq. (10)), vs. time for solar cycle 23. Both figures have the same colour-coding for time.

$\nu_{\max} = 3090\,\mu$Hz would instead yield a smaller slope of 16.57. The changes in oscillation frequencies are due to both the reduction of the radius and the altered stratification of the independent variables. The latter has the stronger effect, in particular for the high-frequency shifts, since we tested this by keeping the radius unchanged, which led to very similar results. Furthermore, for the higher angular degrees modes of $l = 1, 2$ and 3, we find very similar slopes with 25.80, 25.92, and 26.01. In Table 2, we list the coefficients of the modified Lorentzian function (Eq. (8)) that result from the fitting for $l = 0$.

To estimate the global impact on the frequency, we determined the probability distribution function of the magnetic field on the solar surface, f_{B_z}, during the different phases of the solar cycle. We determined f_{B_z} for solar cycle 23 (Carrington rotation numbers from 1909 till 2057, i.e. between the years 1996 and 2008) from synoptic (radially corrected) magnetograms observed by SOHO/MDI[1] (see Fig. 14a). We computed the histograms for 100 bins from the logarithm of the absolute magnetic field strength values. As expected, during the ascending phase of cycle 23, the probability of the magnetic field strength increases at higher field strength, which reduces the probabilities at lower B_z (the total probability is unity). The opposite is true for the declining phase.

Then, with the linear response function (Eq. (9)), we can determine the total shift by integrating the probability distribution function of the surface magnetic field, f_{B_z}, over the magnetic field strength,

$$\delta\nu_{nl}\,(t) \;=\; \frac{1}{B_{z,\max}} \int_0^{B_{z,\max}} \delta\nu^*_{n0}(B_z, t) f_{B_z}(B_z, t)\,\mathrm{d}B_z. \qquad (10)$$

We calculated the total shift (Eq. (10)) for solar cycle 23, which is shown in Fig. 14b. The total shift is largest during the maximum (2002), leading to a shift of $\sim 0.2\,\mu$Hz. Chaplin et al. (2004) considered the frequency shifts for different phases during solar cycles 22 and 23. For the low-angular degree $l = 0/2$ at the solar activity maximum they found a mean shift around $\sim 0.2/0.4\,\mu$Hz. We found very good agreement with our theoretical results. However, we did not find a strong dependence on angular degree mode. From 3D MHD models for stars other than the Sun, the linear response functions, $\delta\nu^*_{nl}$, can be predicted. This opens the possibility of inferring their magnetic field distribution function, f_{B_z}, at their surface, by comparing and matching f_{B_z} to observations of their stellar cycles.

[1] Retrieved from http://soi.stanford.edu

Table 2. Coefficients α and β for the modified Lorentzian function (Eq. (8)) shown in Fig. 12.

$B_{z,0}$	α	β	$B_{z,0}$	α	β
50 G	0.278	5.940	800 G	10.014	4.888
100 G	0.576	5.885	900 G	9.103	5.290
200 G	2.527	4.369	1000 G	10.242	5.322
300 G	2.799	5.384	1100 G	10.893	5.254
400 G	4.912	4.917	1200 G	12.018	5.180
500 G	5.785	3.755	1300 G	11.711	5.503
600 G	6.930	4.670	1400 G	11.391	5.309
700 G	7.249	4.848	1500 G	15.675	5.076

4. Conclusions

The turbulent expansion that elevates the depth-scale and reduces the density stratification is very important for matching the observed solar oscillation frequencies more accurately. On the other hand, the differences in the stratification of the adiabatic exponent are often very small, therefore, the their effects on on the oscillation frequencies are accordingly less important. Furthermore, instead of correcting for the frequencies, the surface of the solar model can be corrected for by expanding

the geometrical depth scale in a depth-dependent way and by reducing the density by the turbulent pressure. This leads to very similar results, as achieved with a ⟨3D⟩ model appended to a 1D model. Considering alternative reference depth scales for determining the spatial averages for the 3D model leads to very similar results, as achieved with averages over geometrical depth. We also found that 1D solar models with higher metallicity result in models that match the low-frequency part that probe the interior better. Finally, we found that strong magnetic fields have a distinct influence by predominantly increasing the high-frequency range and that the linear response is able to reproduce the solar activity cycles properly.

Acknowledgements. This work was supported by a research grant (VKR023406) from VILLUM FONDEN.

References

Asplund, M., Grevesse, N., & Sauval, A. J. 2005, in Cosmic Abundances as Records of Stellar Evolution and Nucleosynthesis, eds. T. G. Barnes III, & F. N. Bash, ASP Conf. Ser., 336, 25
Asplund, M., Grevesse, N., Sauval, A. J., & Scott, P. 2009, ARA&A, 47, 481
Ball, W. H., & Gizon, L. 2014, A&A, 568, A123
Basu, S., Chaplin, W. J., Elsworth, Y., New, R., & Serenelli, A. M. 2009, ApJ, 699, 1403
Beeck, B., Collet, R., Steffen, M., et al. 2012, A&A, 539, A121
Böhm-Vitense, E. 1958, Z. Astrophys., 46, 108
Chaplin, W. J., Elsworth, Y., Isaak, G. R., Miller, B. A., & New, R. 2004, MNRAS, 352, 1102
Christensen-Dalsgaard, J. 2002, Rev. Mod. Phys., 74, 1073
Christensen-Dalsgaard, J. 2008, Astrophys. Space Sci., 316, 113
Christensen-Dalsgaard, J., Dappen, W., Ajukov, S. V., et al. 1996, Science, 272, 1286
Ferguson, J. W., Alexander, D. R., Allard, F., et al. 2005, ApJ, 623, 585
Grevesse, N., & Noels, A. 1993, in Origin and Evolution of the Elements, eds. N. Prantzos, E. Vangioni-Flam, & M. Casse, 15
Grevesse, N., & Sauval, A. J. 1998, Space Sci. Rev., 85, 161
Gustafsson, B., Edvardsson, B., Eriksson, K., et al. 2008, A&A, 486, 951
Iglesias, C. A., & Rogers, F. J. 1996, ApJ, 464, 943
Lazrek, M., Baudin, F., Bertello, L., et al. 1997, Sol. Phys., 175, 227
Magic, Z., Serenelli, A., Weiss, A., & Chaboyer, B. 2010, ApJ, 718, 1378
Magic, Z., Collet, R., Asplund, M., et al. 2013a, A&A, 557, A26
Magic, Z., Collet, R., Hayek, W., & Asplund, M. 2013b, A&A, 560, A8
Mihalas, D., Dappen, W., & Hummer, D. G. 1988, ApJ, 331, 815
Rogers, F. J., Swenson, F. J., & Iglesias, C. A. 1996, ApJ, 456, 902
Rosenthal, C. S., Christensen-Dalsgaard, J., Nordlund, A., Stein, R. F., & Trampedach, R. 1999, A&A, 351, 689
Sonoi, T., Samadi, R., Belkacem, K., et al. 2015, A&A, 583, A112
Stein, R. F., & Nordlund, A. 1998, ApJ, 499, 914
Trampedach, R. 1997, Master's Thesis, Aarhus University
Trampedach, R., Stein, R. F., Christensen-Dalsgaard, J., Nordlund, Å., & Asplund, M. 2014, MNRAS, 442, 805
Weiss, A., & Schlattl, H. 2008, Astrophys. Space Sci., 316, 99